October 23, 2019

Effects of physiological parameter evolution on the dynamics of tonic-clonic seizures

Farah Deeba[1,2,3*], Paula Sanz-Leon[1,2], and P. A. Robinson[1,2]

1 School of Physics, University of Sydney, NSW 2006, Australia

2 Center for Integrative Brain Function, University of Sydney, NSW 2006, Australia

3 Department of Physics, Dhaka University of Engineering and Technology, Gazipur 1700, Bangladesh

* farah.deeba@sydney.edu.au

Abstract

The temporal and spectral characteristics of tonic-clonic seizures are investigated using a neural field model of the corticothalamic system in the presence of a temporally varying connection strength between the cerebral cortex and thalamus. Increasing connection strength drives the system into ~ 10 Hz seizure oscillations once a threshold is passed and a subcritical Hopf bifurcation occurs. In this study, the spectral and temporal characteristics of tonic-clonic seizures are explored as functions of the relevant properties of physiological connection strengths, such as maximum strength, time above threshold, and the ramp rate at which the strength increases or decreases. Analysis shows that the seizure onset time decreases with the maximum connection strength and time above threshold, but increases with the ramp rate. Seizure duration and offset time increase with maximum connection strength, time above threshold, and rate of change. Spectral analysis reveals that the power of nonlinear harmonics and the duration of the oscillations increase as the maximum connection strength and the time above threshold increase. A secondary limit cycle at ~ 18 Hz, termed a saddle-cycle, is also seen during seizure onset and becomes more prominent and robust with increasing ramp rate. If the time above the threshold is too small, the system does not reach the

10 Hz limit cycle, and only exhibits 18 Hz saddle-cycle oscillations. It is also seen that the times to reach the saturated large amplitude limit-cycle seizure oscillation from both the instability threshold and from the end of the saddle-cycle oscillations are inversely proportional to the square root of the ramp rate.

Author Summary

Epilepsy, which is characterized by recurrent seizures, affects around 1% of the world population at some point in their lives. Tonic-clonic seizures are the most commonly encountered primary generalized seizures and it is widely considered that they can be induced by an increase in the connection strength between the cerebral cortex and the thalamus. In this paper, we analyze the detailed dynamics of tonic-clonic seizures along with their dependence on the parameters of the changing connection strength. We study the relationship of the seizure onset, offset, oscillation strength, and oscillation frequency to the duration, amplitude, and rate of change of the connection strength. A detailed understanding of the dynamics and their dependence on the physiological parameters of the brain may explain the variability of seizure dynamics among patients. It may also help to constitute successful seizure prediction.

Introduction

Tonic-clonic seizures, formerly known as grand mal seizures, are the most frequently encountered generalized seizures [1]. These seizures have a tonic phase, which is characterized by an initial increase in tone of certain muscles, followed by a clonic phase, which involves bilateral symmetric jerking of the extremities [2]. Tonic-clonic seizures have markedly different pre- and post-ictal electroencephalograms (EEG) and typically last 1 to 3 minutes. Primary generalized seizures, which is one of the most commonly seen seizures, begin simultaneously across the whole cortex [1].

A number of authors have investigated the mechanisms of seizures using the neural network and neural field approaches [3–13]. Many authors have proposed that transitions from healthy state to the seizure state occur via bifurcations upon changing physiological parameters [3–9, 12, 13]. For example, depending on the instability region,

increasing excitatory connection strengths between cortex and thalamus drives the system into ~ 10 Hz and ~ 3 Hz seizure oscillations via a subcritical and supercritical Hopf bifurcation, respectively, once a critical value (i.e., a threshold) is passed [3–9, 12, 13]. Results from *in vivo* studies have provided evidence that changes in corticothalamic connection strengths can induce seizures [12, 14–16], which possibly occur due to a key cellular event triggered by $GABA_B$ (metabotropic transmembrane receptors for gamma-aminobutyric acid) mediated mechanisms underlying the reduction of the threshold for Ca^{2+} spikes [1, 2] due to the effects of drugs, excess or deficiency of neurotransmitters or neuromodulators [1, 2, 17]. However, the detailed dynamics of generalized tonic-clonic seizure including its dependence to the changing profile of the corticothalamic connection strength have never been studied in detail. The dependence of the spectral characteristics like the frequencies of the oscillations on the parameters of the changing connection strength have also not been studied.

In this study, we apply a widely used neural field model of the corticothalamic system to study the dynamics of tonic-clonic seizures [3–5, 7, 8, 18–20]. Neural field theory (NFT) is a continuum approach that predicts the average dynamics of large numbers of neurons [21, 22]. The specific model used here [23–26] has reproduced and unified many observed features of brain activity based on the physiology, including evoked response potentials [27], activity spectra [28], arousal state dynamics, age-related changes in the physiology of the brain [29], and many other phenomena [3–5, 7, 8, 18–20, 30–32]. The above NFT model has also been used in seizure studies [3–5, 7], where it has successfully unified features of tonic-clonic and absence seizures [3–5, 7], and explain the dependence of the dynamics and interictal oscillations during absence seizures on the parameters of the changing connection strength between the cortex and the thalamus [33, 34]. Previous studies have shown that a gradual increase of the connection strength between the cortex and thalamus near the alpha instability boundary shown in [8] in this model can initiate nonlinear dynamics whose characteristics closely resemble those of tonic-clonic seizures as a result of a subcritical Hopf bifurcation that destabilizes the ~ 10 Hz alpha resonance [3, 4, 19, 31]. Changes in other connection strengths also introduce similar dynamics because of the universality properties of the Hopf bifurcation [12].

The general property and bifurcation mechanism of the resultant tonic-clonic seizure

has been studied in detail in [3]. However, the impact of underlying parameter changes of the corticothalamic connectivity strength on tonic-clonic seizure onset, dynamics, and termination have not been studied in detail. In particular, an extensive study like [33] on the dependence of the onset and termination of tonic-clonic seizure on the temporal form of the connection strength is necessary to understand the variability in seizure events, such as difference in the onset time and duration among different subjects, and to help lay the foundations for tonic-clonic seizure control strategies. These analysis are also necessary to explain the changes in harmonic structures seen in previous studies [35–37] during seizure. In sort, the aims are to understand the effects of physiological parameters on the temporal and spectral characteristics of seizure dynamics, including saddle-cycle oscillations [19].

The outline of this paper is as follows: In the Results, we explore the general characteristics of seizure as well as the dependence of seizure dynamics on the temporal variation of connection strength. In the Discussion, we provide a summary and discuss possible applications of our outcomes and finally, in the Methods section, we present the corticothalamic neural field model along with the temporal variation function and the numerical methods.

Results

In this section we investigate the dynamical characteristics of model tonic-clonic seizures as well as the effects of the temporal variation of the corticothalamic connection strength, ν_{se} on the dynamics. For the investigation of general characteristics, we keep a constant maximum connection strength $\nu_{\max}$, characteristic duration $t_2 - t_1$, and characteristic rise time Δ, and all other parameters listed in Table 1.

To investigate the effect of the variation of ν_{se} on seizure dynamics we vary $\nu_{\max}$, Δ, and $t_2 - t_1$ individually by keeping all other parameters constant. Figure 1(a) shows the variation of ν_{se} with time for the parameters values specified in Table 1.

General characteristics of tonic-clonic seizures

Three main regions are distinguished according to the dynamics of the cortical activity ϕ_e (cortical excitatory field) as illustrated in Fig. 1(b): Region I from $0 - 50$ s is the

pre-ictal state when ν_{se} is too small to initiate seizure-like oscillations; Region II from $125 - 175$ s is the ictal state when ν_{se} is around its maximum value, $\nu_{\max}$, and the system oscillates with maximum amplitude; and Region III from $250 - 330$ s is the post-ictal state, where ν_{se} returns to its baseline value, and oscillations start decreasing in amplitude until they completely cease.

Figures 1(c) and (d) show the zoomed seizure onset and offset, respectively, which are the transitions from Region I to II, and from Region II to III, respectively.

The normalized power spectrum in Region II is shown in Fig. 1(e). Figure 1(e) shows a dominant resonance at ~ 10 Hz with multiple harmonics in Region II, where power decreases gradually with frequency.

Dynamics of seizure onset

Figure 1(b) shows that in Region I, the system remains in the steady state because ν_{se} is below the bifurcation threshold. A small increase in ϕ_e due to the increase of ν_{se} is also seen in this region. At $t = t_\theta$, which is the time at which ν_{se} crosses the linear instability threshold, the fixed point loses its stability, and ~ 18 Hz oscillations appear. The first few oscillations are too small to be distinguished on this scale, but their envelope increases exponentially until $t = t_{sc}$, when the trajectory spirals further outwards to a large amplitude 10 Hz limit cycle, as seen in Fig. 1(c); these 18 Hz oscillations are termed saddle-cycle oscillations because they are due to a saddle cycle located between the stable steady state and the stable large amplitude limit cycle attractor. The envelope of the 10 Hz oscillations continues to increase from $t = t_{sc}$ until $t = t_{lc}$, when the system reaches the large amplitude limit cycle. At $t \approx t_{lc}$, the amplitude of the oscillations overshoots because ν_{se} is still rapidly increasing. Then, the amplitude of the oscillations increases gradually until $\nu_{se} = \nu_{\max}$ in Region II, then decreases.

Figure 1(c) shows a clearer view of saddle-cycle oscillations, and times t_{sc} and t_{lc}; where we define t_{lc} to be the point of inflection.

Dynamics of seizure offset

In Fig. 1(d), we see that the amplitude of the oscillations decreases gradually from its peak during the ramp down of ν_{se}. More specifically, at $t = t_{lc2}$, when ν_{se} crosses the offset bifurcation threshold $\nu_{lc2} = 0.98$ mV s [3], the large limit cycle loses stability and

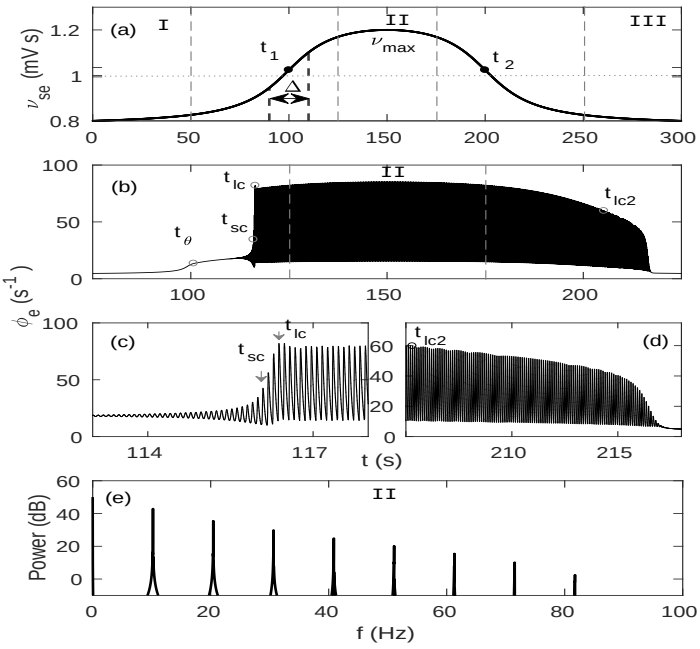

Fig 1. Corticothalamic dynamics for temporally varying ν_{se}, with $\Delta = 20$ s and rest of the parameters shown in Table 1. (a) Temporal profile of ν_{se} varying from ν_0 to $\nu_{\max}$ and back. Three different regions are identified as: I = pre-ictal state, II = ictal state, and III = post-ictal state. (b) Cortical excitatory field ϕ_e vs. t, showing a 10 Hz spike-wave oscillation. Individual oscillations can not be distinguished on this scale. (c) Zoom of ϕ_e at seizure onset. (d) Zoom of ϕ_e at seizure offset. (e) Power spectrum of ϕ_e in Region II. An arbitrary dB scaling is used because clinical EEG recordings involve additional attenuation by structures between the cortex and the electrode, which we do not model here.

the oscillation amplitude decreases steeply to approach the stable steady state in Region III.

Differences between onset and offset dynamics

Comparing Fig. 1(c) with Fig. 1(d), we see that $\nu_\theta > \nu_{lc2}$, as expected for transitions due to a subcritical Hopf bifurcation. This is further seen in Fig. 2, where we see that the system bifurcates from the fixed point at $\nu_{se} = \nu_\theta$ and reaches the saturated large amplitude attractor at $\nu_{se} = \nu_{lc}$. As ν_{se} decreases, the large amplitude attractor becomes unstable at $\nu_{se} = \nu_{lc2}$ and the system returns toward the fixed point.

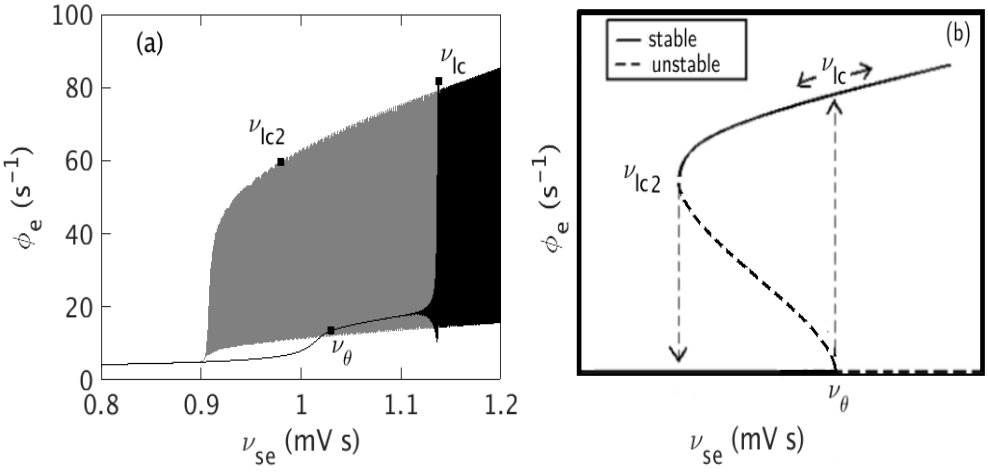

Fig 2. Hysteresis between seizure onset and offset. (a) ν_{se} vs. ϕ_e. Black color shows the variation of ϕ_e during ramp up, i.e. during onset, and gray color shows the variation of ϕ_e during ramp down, i.e. during offset. (b) A schematic diagram of the hysteresis. Solid lines show stable states and dashed lines show unstable ones.

Analytical prediction of onset and offset transition times

Paralleling the analytic prediction of the characteristic time required to develop absence seizures [33], we next predict characteristic tonic-clonic onset and offset times.

For $\nu(t) \approx \nu_\theta$, the oscillation amplitude A obeys

$$\frac{\mathrm{d}A}{\mathrm{d}t} \approx C\,[\nu(t) - \nu_\theta]\,A, \tag{1}$$

where C is a constant, and $\nu(t)$ is the instantaneous value of ν_{se}. Because ν_{se} only varies with time t, we can make the approximation $\nu(t) - \nu_\theta \approx c(t - t_\theta)$ near the threshold, when the oscillation starts at A_θ. This yields

$$A = A_\theta \exp\left[c\,(t - t_\theta)^2/2\right]. \tag{2}$$

with $c = C d\nu(t)/dt|_{t=t_\theta}$; then $A = A_{lc}$ at $t = t_{lc}$

$$\exp\left[\frac{c(t_{lc} - t_\theta)^2}{2}\right] = \frac{A_{lc}}{A_\theta}, \tag{3}$$

$$t_{lc} - t_\theta = \frac{k}{\sqrt{d\nu(t)/dt|_{t=t_\theta}}}, \tag{4}$$

where $k = [(2/C)\ln(A_{lc}/A_\theta)]^{1/2}$. Similar analysis predicts that the transition time $t_{lc} - t_{sc}$ from the saddle-cycle attractor to the larger limit cycle also follows this scaling.

The decrease of oscillation amplitude during the ramp down period can be approximated as

$$\frac{\mathrm{d}A}{\mathrm{d}t} \approx -C' \left[\nu(t) - \nu_{lc2}\right] A, \tag{5}$$

$$\frac{\mathrm{d}A}{\mathrm{d}t} = -C'' \left[t - t_{lc2}\right] A, \tag{6}$$

where C' and C'' are constants, and t_{lc2} is the offset bifurcation threshold as mentioned in previous sections. This yields

$$\ln\left(A/A_{lc2}\right) = -\frac{C''}{2}\left(t - t_{lc2}\right)^2, \tag{7}$$

which indicates a superexponential decrease during seizure offset.

Dynamics during ictal state plateau

Figure 3 shows the phase space trajectory of ϕ_e for the default parameters in Table 1, except $\Delta = 2$ s, which we use to see the saddle-cycle attractor more clearly. Figure 3(a) shows the trajectory of ϕ_e on the ϕ_e - $\mathrm{d}\phi_e/\mathrm{d}t$ plane. In the left edge of the figure, we see the evolving fixed point, which first appears as straight line and then moves towards the right with increasing ν_{se}. Once the system crosses the linear instability threshold, the fixed point becomes unstable and the trajectory spirals out to a large amplitude limit cycle attractor via an unstable saddle-cycle attractor. The amplitude of the large attractor increases gradually until $\nu_{se} = \nu_{\max}$, then decreases until ν_{lc2}, where it becomes unstable and the system spirals back to the stable fixed point; no saddle-cycle is seen during the inward spiral. Three segments of the trajectory are shown in Figs 3(b) – (d), to clarify these dynamics. Figure 3(b) shows ϕ_e spiraling outward from the steady state to the saddle-cycle attractor with amplitude ≈ 30 s^{-1}. Figure 3(c) shows the outward spiral from the saddle cycle to the limit cycle attractor with amplitude ≈ 90 s^{-1}. Figure 3(d) shows the inward spiral during ramp down of ν_{se}.

Figure 4 shows the dynamic spectrum of ϕ_e from Fig. 1(b). A sudden appearance of 10 Hz oscillation with multiple harmonics at $t = t_\theta$ is seen. These harmonics resemble with the harmonics seen in [3], both experimentally and theoretically. The power of the harmonics decreases with harmonic number and their duration decreases slightly. We

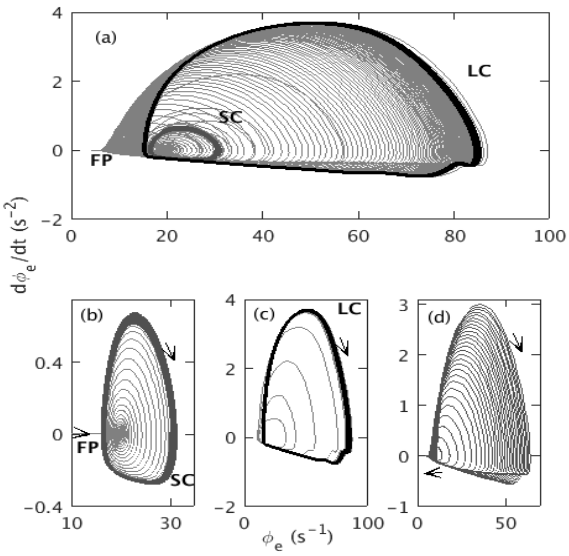

Fig 3. Phase space trajectory of ϕ_e for $\Delta = 2$ s, and rest of the default parameters as in Table 1. (a) Trajectory from from $t = 5$ s to $t = 295$ s. Initial small straight line labeled with FP corresponds to the evolving fixed point; small dark gray segment labeled with SC corresponds to the saddle-cycle attractor; black segment labeled with LC corresponds to the large amplitude limit cycle attractor. The fixed point and center of the clockwise limit cycle trajectory move from left to right during ramp up and right to left during ramp down. (b) Trajectory from $t = 104$ s to $t = 107$ s. (c) Trajectory from $t = 114.5$ s to $t = 150$ s. (d) Trajectory from $t = 200$ s to $t = 295$ s.

find a frequency broadening during the seizure onset at ~ 113.5 s, due to the rapid change of the amplitude of the oscillations. Frequency broadening of the first few harmonics during seizure offset is also seen, and there is a slight frequency drop.

Dynamics of corticothalamic seizure propagation

Figures 5 (a) and (b) show the time series of the fields ϕ_r during onset and offset, respectively. Similarly, Figs 5 (c) and (d) show the time series of the fields ϕ_s during onset and offset.

From these plots we observe that (i) during onset ϕ_r reaches much higher amplitudes than ϕ_e; and, (ii) the ratio between the amplitude of the small oscillations that develop after crossing the bifurcation and the amplitude of the saturated limit cycle is smaller for ϕ_e than it is for ϕ_r and ϕ_s.

In order to study the interplay among ϕ_e, ϕ_r, and ϕ_s in more detail, we plot their limit cycle phase space trajectories and time series at $\nu_{se} \approx \nu_{\max}$ in Fig. 6. Figures 6(a)

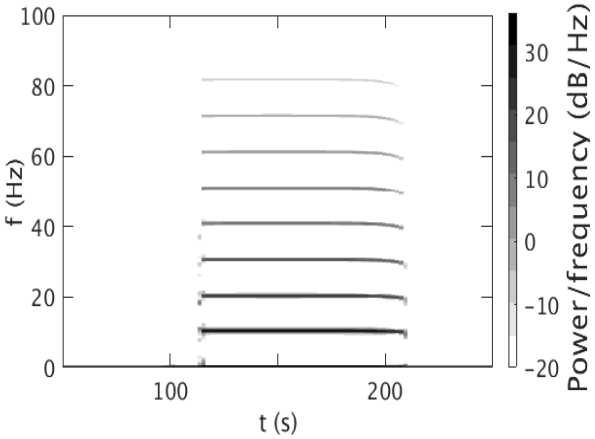

Fig 4. Dynamic spectrum for $\nu_{\max} = 1.2$ mV s with the parameters in Table 1. A Hanning window of 600 data points, an overlap of 200 points, and sampling frequency of 200 Hz was used. The color bar shows the dB scale.

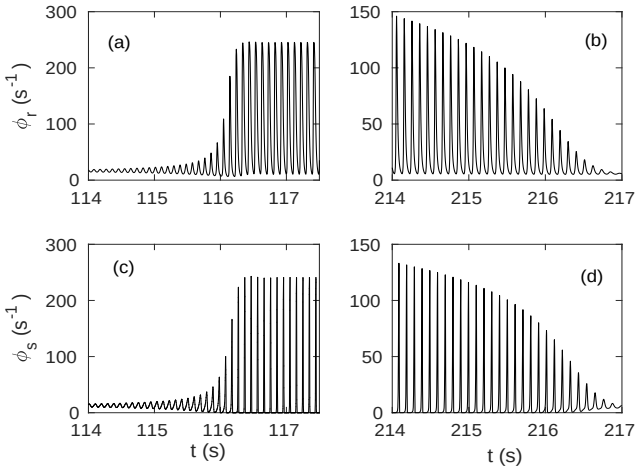

Fig 5. Time series of fields during seizure onset and offset: (a) ϕ_r at seizure onset. (b) ϕ_r at seizure offset. (c) ϕ_s at seizure onset. (d) ϕ_s at seizure offset.

and (b) show the time series and phase space trajectory of ϕ_e, respectively. Figures 6(c) and (d) show the time series and phase space trajectory of ϕ_r, respectively. A $t_0/2$ time shift between the peaks of ϕ_e and ϕ_r is seen due to the propagation delay between these populations. We also see a wide minimum between two successive peaks of ϕ_r. The phase space in Fig. 6(d) shows similar trajectory to Fig. 6(d), but with greater amplitude. Figures 6(e) and (f) show the time series and phase space of ϕ_s, respectively, and they show an equal amplitude but wider peak than Figs 6(c) and (d). Figure 6 shows that all three fields exhibit slightly different trajectories, with the higher amplitudes of ϕ_r and ϕ_s near the maximum firing rate.

Close examination of Fig. 6 reveals the signal flow through the populations. A peak of ϕ_e reaches ϕ_r and ϕ_s simultaneously $t_0/2$ later. The peak of ϕ_e coincides approximately with the bottom of the trough of ϕ_r, and a positive excitation with the maximum firing rate appears, which suppress ϕ_s. This suppression then reduce the excitation of ϕ_e a time $t_0/2$ later and causes an exponential decay. A negative perturbation to ϕ_e results, which then propagates to the thalamus again and reduces the excitation of ϕ_r after a further time $t_0/2$, which allows a positive excitation of ϕ_s almost immediately. This positive excitation then flows to ϕ_e and initializes the next cycle of the loop.

In molecular level, the imbalance between inhibitory and excitatory conductances induced by blocking synaptic and voltage-gated inhibitory conductances, or by activating synaptic and voltage-gated excitatory conductances incorporates the positive feedback, which leads to seizures [17, 38]. Seizures are suppressed by the opposite manipulations: increasing inhibition or decreasing excitation [17, 38].

Impact of temporal variation of ν_{se} on seizure dynamics

In this section, we investigate the effects of the temporal variation of ν_{se} on the model seizure dynamics by varying the maximum connection strength $\nu_{\max}$, duration $t_2 - t_1$, and rise time Δ, holding all other parameters at the values in Table 1.

We first analyze the impact of the variation of ν_{se} on the overall dynamics of ϕ_e, as shown in Fig. 7. For $\nu_{\max} = 1$ mV s in Fig. 7(a), ϕ_e increases with ν_{se} as shown in Fig. 16, then returns smoothly to the initial steady state value as ν_{se} returns to ν_0.

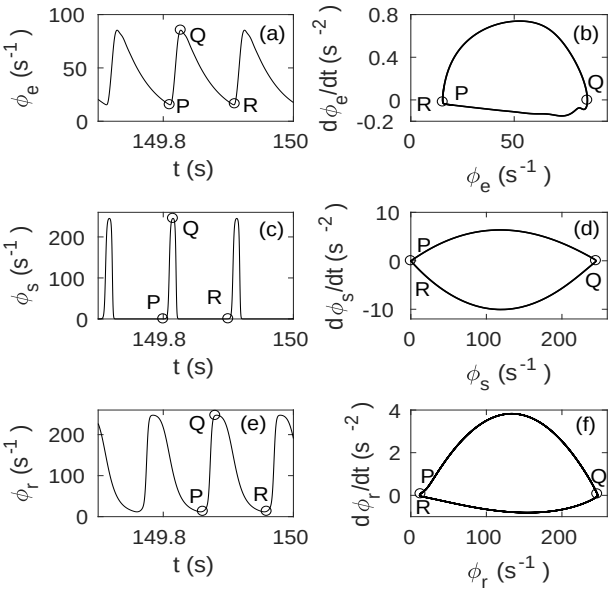

Fig 6. Mid-seizure limit cycle dynamics of ϕ_e, ϕ_s, and ϕ_r from $t = 149.7$ s to $t = 150$ s with other parameters as in Table 1. (a) Time series of ϕ_e at $\nu_{se} \approx \nu_{\max}$. (b) Phase space trajectory of ϕ_e. (c) ϕ_r at $\nu_{se} \approx \nu_{\max}$. (d) Trajectory of ϕ_r. (e) ϕ_s at $\nu_{se} \approx \nu_{\max}$. (f) Trajectory of ϕ_s. P and R are successive minimums and Q is the intermediate maximum.

Figures 7(b) and (c) show that increasing $\nu_{\max}$, yields periodic oscillations of increasing magnitude as corticothalamic feedback strengthens; oscillations also start earlier and are damped away later because the system crosses onset threshold earlier and offset threshold later for higher $\nu_{\max}$. However, the system does not return to its initial steady state for $\nu_{\max} > 1.542$ mV s; instead it moves to the high firing steady state of Fig. 16.

Figures 7(d) – (f) show the effects of varying ramp width Δ from 2 s to 60 s. Figure 7(d) shows that for the step-like variation of ν_{se} for $\Delta = 2$ s, the oscillations rapidly reach maximum amplitude after the transition to the large amplitude attractor and also decrease sharply from their maximum to the initial steady state once the system crosses the threshold during ramp down. Figures 7(e) and (f) show that the slower ramp for larger Δ implies that the amplitude of the oscillations during seizure onset and offset decreases more gradually.

Figures 7(g) – (i) show the effects of variation of the characteristic time $t_2 - t_1$ from 20 s to 100 s. As expected, the duration of seizure oscillations increases with $t_2 - t_1$.

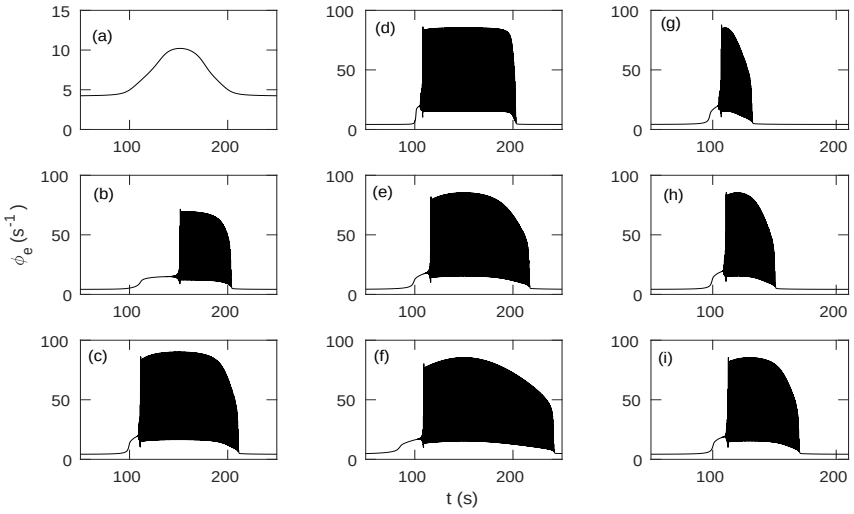

Fig 7. Time series for different temporal profiles of ν_{se}, with other parameters as in Table 1. (a) ϕ_e vs. t for $\nu_{\max} = 1$ mV s. Individual oscillations cannot be distinguished. (b) $\nu_{\max} = 1.05$ mV s. (c) $\nu_{\max} = 1.25$ mV s. (d) $\Delta = 2$ s. (e) $\Delta = 20$ s. (f) $\Delta = 60$ s. (g) $t_2 - t_1 = 20$ s. (h) $t_2 - t_1 = 40$ s. (i) $t_2 - t_1 = 60$ s.

Seizure onset time

Figure 8 quantifies the effects of $\nu_{\max}$ and Δ on seizure onset. We do not revisit the variation with $t_2 - t_1$ because its effects were already discussed in the previous subsection.

Figure 8(a) shows that t_θ decreases with increasing $\nu_{\max}$, because the system reaches ν_θ earlier for a higher $\nu_{\max}$. Figure 8(b) shows the variation of t_θ with Δ. For $\Delta < 10$ s, t_θ increases slightly with Δ, because due to the high rate of change, ν_{se} rapidly approaches its maximum, crossing all the bifurcation values. At longer $\Delta \geq 10$ s, the temporal profile of ν_{se} becomes smooth and flat topped like Fig. 1(a) and ν_{se} gradually ramps up to the bifurcation point, so the system crosses the threshold later for a larger Δ, resulting in a decrease in t_θ.

Dynamic spectrum

In this section we discuss the effects of changing the temporal profile of ν_{se} on the power spectrum of ϕ_e and use its evolution to further clarify the occurrence of saddle cycles.

Figure 9(a) shows the dynamic spectrum for $\nu_{\max} = 1.05$ mV s. During the seizure, we observe a peak at approximately ~ 10 Hz with several harmonics. We also find lower

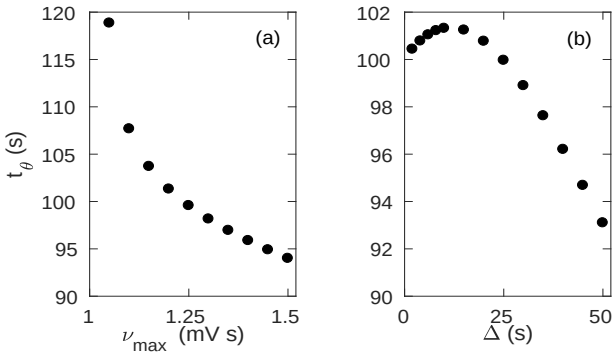

Fig 8. Effects of temporal variation of ν_{se} on seizure onset with parameters as in Table 1. (a) t_θ vs. $\nu_{\max}$. (b) t_θ vs. Δ.

frequency drop and broadening during seizure onset and offset as in Fig. 4. Figure 9(b) shows that for $\nu_{\max} = 1.15$ mV s, harmonics have greater duration and power than Fig. 9(a); frequency broadening is also more prominent. Figure 9(c) shows that for $\nu_{\max} = 1.55$ mV s, there is no oscillation after $t = 143.52$ s. A detailed investigation shows that the power of the peaks increases significantly with $\nu_{\max}$ and $t_2 - t_1$, but decreases slightly with Δ, especially at higher order harmonics. A small peak around 205 s shows that the system returns to the initial steady state via small oscillation after it crosses the offset bifurcation.

Characteristic transition times

In this section we test the analytic prediction made in earlier sections. Figure 10(a) shows $t_{lc} - t_\theta$ vs. $(d\nu_{se}/dt)^{-1/2}$. A least-squares fit to these data yields

$$t_{lc} - t_\theta = a(d\nu_{se}/dt)^{-\frac{1}{2}} - b, \tag{8}$$

with $a = (0.042 \pm 0.004)$ V$^{1/2}$ s and $b = (0.9 \pm 1.4)$ s, which is consistent with Eq. (4). Figure 10(b) shows $(d\nu_{se}/dt)^{-1/2}$ vs. $t_{lc} - t_{sc}$. A least-squares fit yields

$$t_{lc} - t_{sc} = a'(d\nu_{se}/dt)^{-\frac{1}{2}} + b', \tag{9}$$

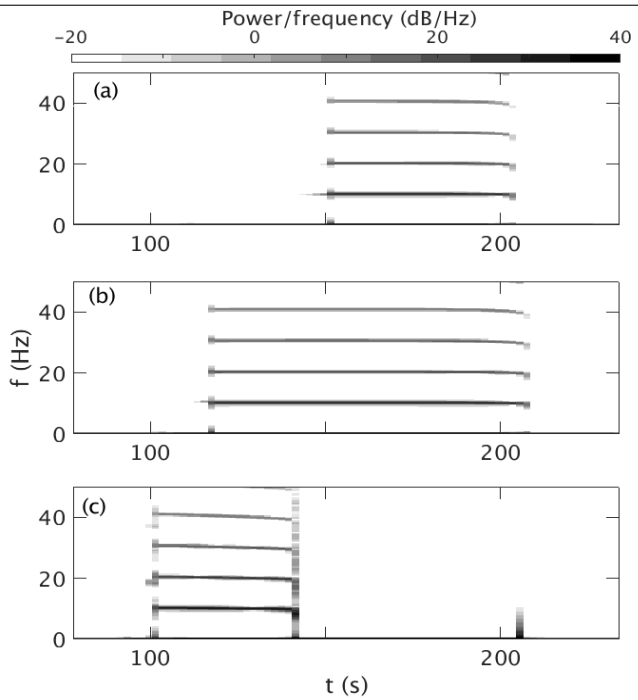

Fig 9. Dynamic spectrum vs. $\nu_{\max}$ for the parameters in Table 1. The power density of the harmonics is calculated using a Hanning window of 600 data points, an overlap of 200 points, and sampling frequency of 200 Hz, the color bar at top shows the dB scale. (a) Dynamic spectrum for $\nu_{\max} = 1.05$ mV s. (b) $\nu_{\max} = 1.15$ mV s. (c) $\nu_{\max} = 1.55$ mV s.

with $a' = (0.003 \pm 0.001)$ $\mathrm{V}^{1/2}$ s and $b' = (0.0 \pm 0.2)$ s, which has the same scaling as Eq. (4).

Figure 10(c) shows $\ln(A/A_{lc2})$ vs. $(t - t_{lc2})^2$ for $\Delta = 10$ s, which follows Eq. (7) until the amplitudes of the oscillations start to decrease super-exponentially towards the steady state. A least-squares fit to the linear decrease yields

$$\ln\left(A/A_{lc2}\right) = -a''\left(t - t_{lc2}\right)^2 - b''. \tag{10}$$

with $a'' = (0.0116 \pm 0.0002)$ s^{-2} and $b'' = (0.018 \pm 0.004)$. The figure shows that the decrease of the envelope follow the linear fit for a relatively short time, after which the decrease becomes steeper. By using Eqs (2) and (3), it can be also shown that decrease within the linear region also follows the same scaling as Eq. (4).

Saddle Cycle

Previously, we mentioned the presence of a small amplitude ~ 18 Hz saddle cycle. The system orbits there for few seconds, then spirals out towards the large amplitude limit

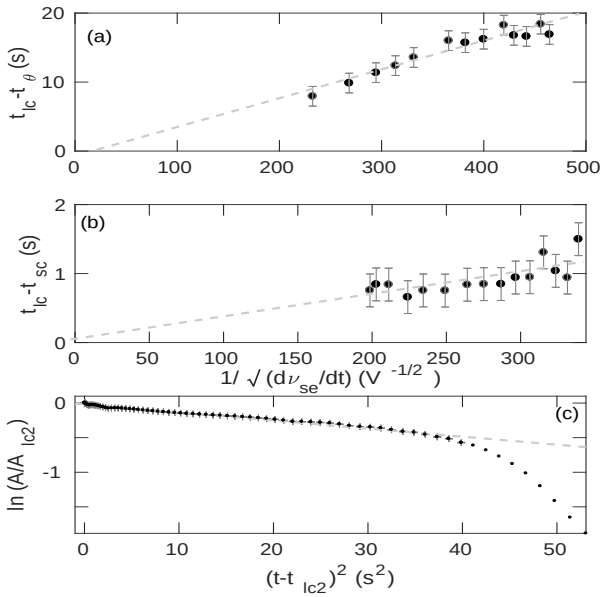

Fig 10. Dependence of seizure transition times on $(d\nu_{se}/dt)^{-1/2}$ with the default parameters as in Table 1 and Δ ranges from 2 s to 50 s. (a) $t_{lc} - t_\theta$ vs. $(d\nu_{se}/dt)^{-1/2}$; (b) $t_{lc} - t_{sc}$ vs. $(d\nu_{se}/dt)^{-1/2}$, and (c) $\ln(A/A_{lc2})$ vs. $(t - t_{lc2})^2$ for $\Delta = 10$ s and time ranges from 190 s to 250 s. Error bar represent uncertainties of the least-squares fits. Points with no error bars are not considered for the least-squares fit.

cycle attractor. However, this saddle-cycle is not observed in all cases, for example, a colose zoom near the onset of all subfigures of Fig. 7 will show that the small amplitude saddle-cycle oscillations like Fig. 1(c) are only prominent in Figs 7(c) and (d). Here, we explore the dependence of the saddle-cycle oscillations on $\nu_{\max}$ and Δ.

Figure 11 shows the variation of saddle-cycle oscillations with respect to $\nu_{\max}$, with other parameters as in Table 1. Figure 11(a) shows the phase space trajectory for $\nu_{\max} = 1.15$ mV s. No saddle-cycle attractor is seen in this figure. Figure 11(b) shows the trajectory for $\nu_{\max} = 1.25$ mV s. A small saddle-cycle attractor is seen between the fixed point and the large amplitude attractor. Figures 11(c) and (d) show the trajectories for $\nu_{\max} = 1.35$ mV s and 1.45 mV s, respectively. The saddle cycle increases in size with $\nu_{\max}$. A similar investigation shows that similar phenomena occur when Δ is varied, with the saddle cycle being most prominent for small Δ, completely disappearing for $\Delta \gtrsim 20$ s.

To understand the relation between the saddle-cycle oscillation and rate of change of ν_{se} more clearly, we calculate the power spectrum for different $\nu_{\max}$ and Δ. Figure 12(a) shows the variation of the power spectrum with $\nu_{\max}$. For a small $\nu_{\max}$, there is no

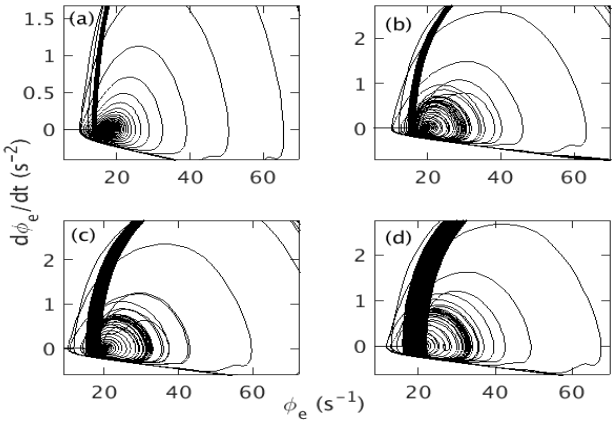

Fig 11. Effects of variation of $\nu_{\max}$ on saddle-cycle with rest of the parameters as in

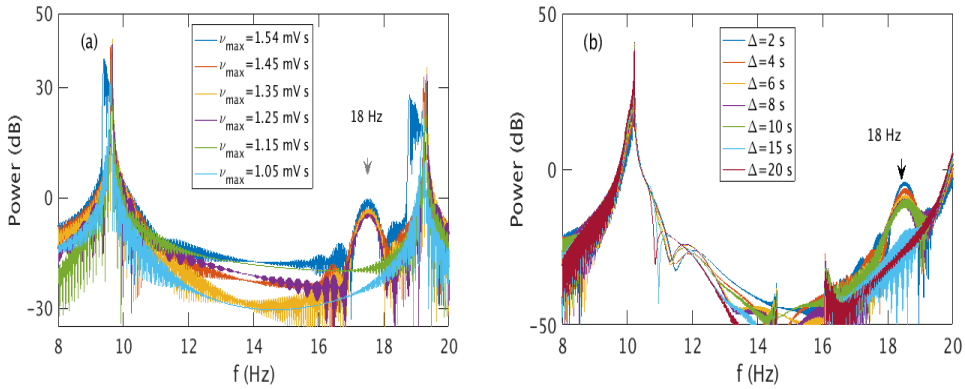

Fig 12. (Color online) Variation in the power of the saddle-cycle oscillations with rest of the parameters in Table 1. (a) Power spectrum vs. $\nu_{\max}$. (b) Power spectrum vs. Δ. Legends show the corresponding values of $\nu_{\max}$ and Δ.

peak around 18 Hz, but a peak at approximately 18 Hz appears when $\nu_{\max} \geq 1.2$ mV s and becomes more prominent and strong with increasing $\nu_{\max}$. Figure 12(b) shows that the power of the peak around 18 Hz decreases with Δ and disappears for $\Delta \gtrsim 20$ s.

These results imply that the presence of saddle-cycle oscillations depends on the rate of change of of ν_{se}. Figure 13 illustrates the presence or absence of saddle-cycle oscillations for 236 different combinations of ν_{se} and Δ as a function of the value of $d\nu_{se}/dt$. When $d\nu_{se}/dt < 7 \times 10^{-3}$ mV, there are no saddle-cycle oscillations; for $d\nu_{se}/dt > 9 \times 10^{-3}$ mV, the system always exhibits saddle-cycle oscillations; while for $7 \times 10^{-3} \lesssim d\nu_{se}/dt \lesssim 9 \times 10^{-3}$ mV, there is a narrow mixed region where the presence of saddle cycle cannot be predicted solely from the rate of change of ν_{se}.

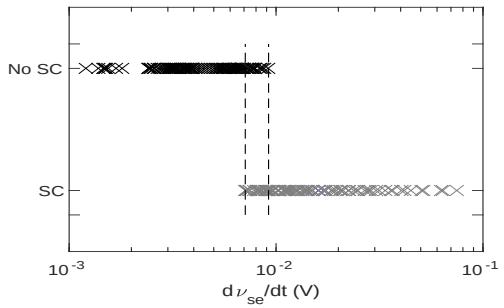

Fig 13. Dependence of saddle-cycle oscillations on $d\nu_{se}/dt$. Gray crosses show the presence of a saddle-cycle and black crosses show its absence.

In order to see why saddle cycles are only seen for high $d\nu_{se}/dt$, we show the time evolution of 10 Hz and 18 Hz frequency peaks for $\Delta = 2$ s and $\Delta = 50$ s in Fig. 14 during seizure onset with other parameters as in Table 1. In Fig. 14(a), for $\Delta = 50$ s and $d\nu_{se}/dt = 0.003$ mV, the 10 Hz peak always rise faster than the 18 Hz peak, and hence, always has more power and dominates the spectrum; no saddle cycles are seen in the trajectory. On the other hand, in Fig. 14(b), for $\Delta = 2$ s and $d\nu_{se}/dt = 0.03$ mV, the 18 Hz peak rises faster than the 10 Hz peak during onset so there is a ~ 2 s window in which the 18 Hz peak dominates and hence, the system is seen to exhibit saddle-cycle oscillations during onset in Fig. 1, after which the 10 Hz peak dominates. Now, since, ν_θ is a the bifurcation threshold and does not depend on the temporal profile, but ν_{lc} depends on the temporal profile and the time to reach the 10 Hz limit cycle (i.e., $t_{lc} - t_\theta$), we conclude that ν_{lc} is the parameter that defines the existence of the saddle cycle. The system will exhibit saddle cycle oscillation only if $\nu_{sc} > \nu_{lc}$ at t_{sc}.

Discussion

We have used an established neural field model of the corticothalamic system [3] to study the dependence of tonic-clonic seizures on the temporal profile of a corticothalamic connection strength ν_{se} that induces seizures. The effects of varying other connection strengths can also be qualitatively predicted using these outcomes because they will exhibit similar dynamics due to the universality properties of the Hopf bifurcation. Also, the function [Eq. (20)] used to vary the connection strength is an approximation of what seems to occur in living systems. This function is an

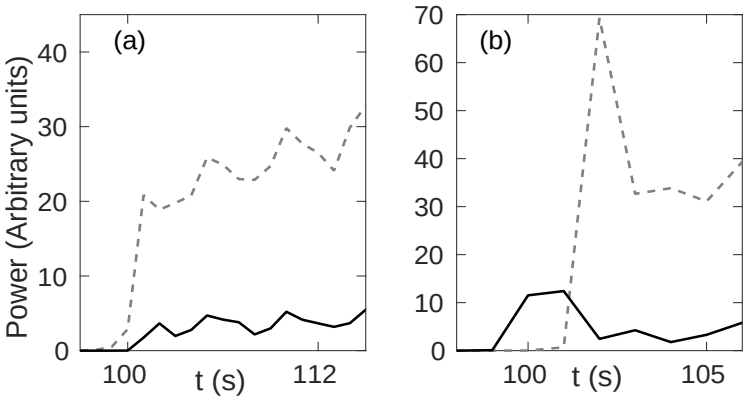

Fig 14. Temporal variation of frequency peaks during seizure onset; black solid line shows the ~ 18 Hz peak; gray dashed line shows the ~ 10 Hz peak with parameters from Table 1. (a) $\Delta = 50$ s; (b) $\Delta = 2$ s.

improvement over previous piece-wise linear functions [3]. The parameters and the shape of Eq. (20) could be customized in the future using experimental data. The key outcomes are:

(i) The system exhibits $\sim$10 Hz limit cycle oscillations once the connection strength crosses the bifurcation threshold of $\nu_\theta = 1.025$ mV s, which is the characteristic frequency of tonic-clonic seizure via a subcritical Hopf bifurcation. The system returns to the resting equilibrium when the connection strength decreases below the offset threshold, $\nu_{lc2} = 0.98$ mV s. The difference in onset and offset bifurcation values causes hysteresis; consistent with previously published results that used piecewise linear variation of ν_{se}, rather than the present more realistic continuous gradual variation.

(ii) For $\nu_{\max} \gtrsim 1.542$ mV, the system moves to another steady state near maximum firing rate and only returns to the initial steady state once ν_{se} returns below an offset threshold.

(iii) The amplitude of ϕ_e increases with the maximum connection strength, $\nu_{\max}$, because an increase of the connectivity strength increases the strength of the positive feedback loop between the cortex and the thalamus.

(iv) Because increasing the maximum connection strength $\nu_{\max}$ increases the amplitudes of the oscillations, it increases the power and the characteristic number of harmonics. The power of the harmonics also increases with the seizure duration $t_2 - t_1$, but decreases slightly with the ramp duration Δ.

(v) The characteristic transition times required to reach the saturated limit cycle oscillation from the seizure threshold or the end of the saddle-cycle oscillations to the steady state are predicted and verified numerically to be inversely proportional to the square root of the rate of change of the connection strength.

(vi) The system can also show transient ~ 18 Hz saddle-cycle oscillation at the beginning of the seizure for high $d\nu_{se}/dt$ before moving to the 10 Hz attractor. These saddle-cycles become more prominent as $d\nu_{se}/dt$ increases; a system with $d\nu_{se}/dt < 7 \times 10^{-3}$ mV never exhibits saddle-cycles, whereas one with $d\nu_{se}/dt > 9 \times 10^{-3}$ mV always does.

Overall, the present study enables the varying spectral and temporal characteristics of seizures to be related to underlying physiological changes of the brain, such as changes in the connection strength between the cortex and the thalamus. The outcomes can be used for explaining the variability of seizure onset properties and seizure frequency across subjects by examining the temporal and spectral characteristics of seizure [39–41]. It may thus be possible to constrain the physiological properties of the corticothalamic connection strength dynamics of a subject by comparing the wave properties of seizure oscillations, such as amplitude, and frequency, with theory. Real-time fitting of the theoretical dynamics to observed waveforms may also be feasible, leading to the possibility of implementing feedback control systems based on the dynamics.

Methods

In this section, we present a brief description of the corticothalamic neural field model used, along with the form of temporal variation of corticothalamic coupling strength [3, 4, 8].

Corticothalamic Field Model

To investigate the dynamics of tonic-clonic seizure, we use the neural field model of the corticothalamic system seen in Fig. 15. In this study we use the same analytical model of [33], but in different parametric regime suitable to study the tonic-clonic seizure. The neural populations are denoted as: e = excitatory cortical; i = inhibitory cortical; s = thalamic relay neurons; r = thalamic reticular nucleus; and n = external inputs. The

dynamical variables within each neural population a are the local mean cell-body potential V_a, the mean rate of firing at the cell-body Q_a, and the propagating axonal fields ϕ_a. The firing rates Q_a are related to the potentials V_a by the response function

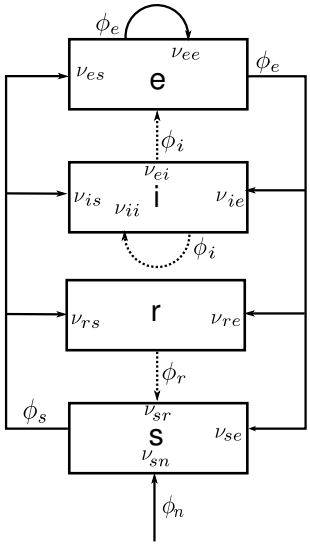

Fig 15. Schematic diagram of the corticothalamic model system. The neural populations shown are cortical excitatory (e), inhibitory (i), thalamic reticular (r), thalamic relay (s), and n = external inputs. The parameter ν_{ab} quantifies the connection to population a from population b. Inhibitory connections are shown with dashed lines.

$$Q_a(\mathbf{r},t) = S[V_a(\mathbf{r},t)], \tag{11}$$

where S is a smooth sigmoidal function that increases from 0 to $Q_{\max}$ as V_a increases from $-\infty$ to ∞, with

$$S(V_a) = \frac{Q_{\max}}{1+\exp[-\pi(V_a-\theta)/\sigma\sqrt{3}]}, \tag{12}$$

where θ is the mean neural firing threshold, σ is the standard deviation of this threshold, and $Q_{\max}$ is the maximum firing rate [3, 8].

In each neural population, firing rates Q_a generate propagating axonal fields ϕ_a that approximately obey the damped wave equation [3, 8]

$$D_a\phi_a(\mathbf{r},t) = Q_a(\mathbf{r},t), \tag{13}$$

where the spatiotemporal differential operator D_a is

$$D_a = \frac{1}{\gamma_a^2}\frac{\partial^2}{\partial t^2} + \frac{2}{\gamma_a}\frac{\partial}{\partial t} + 1 - r_a^2\nabla^2, \tag{14}$$

where $\gamma_a = v_a/r_a$ is the damping rate, r_a and v_a are the characteristic range and conduction velocity of axons of type a, and ∇^2 is the Laplacian operator. The smallness of r_i, r_s, and r_r enables us to set $\gamma_a \simeq \infty$ except for $a = e$. The cell-body potential V_a results after postsynaptic potentials have propagated through the dendritic tree and then been summed as their resulting currents charge the soma. For excitatory and inhibitory neurons within the cortex, this is approximated via the second-order delay-differential equation [8]

$$D_\alpha V_a(\mathbf{r}, t) = \nu_{ae}\phi_e(\mathbf{r}, t) + \nu_{ai}\phi_i(\mathbf{r}, t) + \nu_{as}\phi_s(\mathbf{r}, t - t_0/2), \tag{15}$$

where $a = e, i$ and the temporal differential operator is given by

$$D_\alpha = \frac{1}{\alpha\beta}\frac{d^2}{dt^2} + \left(\frac{1}{\alpha} + \frac{1}{\beta}\right)\frac{d}{dt} + 1. \tag{16}$$

The quantities α and β in Eq. (16) are the inverse decay and rise times, respectively, of the cell-body potential produced by an impulse at a dendritic synapse. Note that input from the thalamus to the cortex is delayed in Eq. (15) by a propagation time $t_0/2$. For neurons within the specific and reticular nuclei of the thalamus, it is the input from the cortex that is time delayed, so

$$D_\alpha V_a(\mathbf{r}, t) = \nu_{ae}\phi_e(\mathbf{r}, t - t_0/2) + \nu_{as}\phi_s(\mathbf{r}, t) + \nu_{ar}\phi_r(\mathbf{r}, t) + \nu_{an}\phi_n(\mathbf{r}, t), \tag{17}$$

where $a = s, r$. The connection strengths are given by $\nu_{ab} = N_{ab}s_{ab}$, where N_{ab} is the mean number of synapses to neurons of type a from type b and s_{ab} is the strength of the response in neurons a to a unit signal from neurons of type b. The final term on the right-hand side of Eq. (17) describes inputs from outside the corticothalamic system. In order to simplify the model we only include the connections shown in Fig. 15, so only 10 of the possible 16 connections between the four neural populations are nonzero [8]. We also assume the random intracortical connectivity and the number of connections

between populations is proportional to the number of synapses [42, 43]. This random connectivity assumption provides $N_{ib} = N_{eb}$ for all b, so $\nu_{ee} = \nu_{ie}$, $\nu_{ei} = \nu_{ii}$ and $\nu_{es} = \nu_{is}$ [30].

Setting all spatial and temporal derivatives in Eqs (12) – (17) to zero determines spatially uniform corticothalamic steady states. The steady state firing rate, $\phi_e^{(0)}$ of ϕ_e is then given by [18]

$$S^{-1}(\phi_e^{(0)}) - (\nu_{ee} + \nu_{ei})\phi_e^{(0)} = \nu_{es} S\Big\{\nu_{se}\phi_e^{(0)} + \nu_{sr} S\Big[\nu_{re}\phi_e^{(0)} + (\nu_{rs}/\nu_{es})\Big(S^{-1}(\phi_e^{(0)}) - (\nu_{ee} + \nu_{ei})\phi_e^{(0)}\Big)\Big] + \nu_{sn}\phi_n^{(0)}\Big\}. \quad (18)$$

The properties of steady states in the corticothalamic model have been studied extensively in [8, 18], and we use the outcomes to identify the stable and unstable regions of the steady state. Figure 16 shows the steady state dependence of $\phi_e^{(0)}$ on ν_{se} with other parameters as in Table 1. It is seen that there are two stable steady state solutions: one corresponds to low mean firing rate and another to very high mean firing rate [18]. The low firing steady state was identified with normal states of brain activity in previous studies [8, 26]. The low firing-rate fixed point loses its stability at $\nu_{se} = \nu_\theta$. A steep increase in $\phi_e^{(0)}$ is seen near ν_i because the increasing ν_{se} push the sigmoid from its minimum by increasing the $\nu_{se}\phi_e^{(0)}$ in Eq. (18), which results in an increase of the gain between the thalamus and the cortex. With further increase of ν_{se}, the system eventually moves to a steady state with near-maximum firing rate. This high firing steady state is beyond the scope of our model because it will lead to effects such as hypoxia, which are not included here.

Temporal Ramping

Brain activity propagates via the coupling of the various neuronal populations. Previous studies have shown that a gradual ramp-up of the coupling strength between the neuronal populations can lead from a stable steady state to periodic seizure oscillations [3, 33]. It is also seen that the dynamical and spectral characteristics of the resultant seizure-like oscillations depend on the physiological properties of the ramp of the coupling strength, such as, the maximum amplitude of the ramp, ramp rate, and characteristic duration [33].

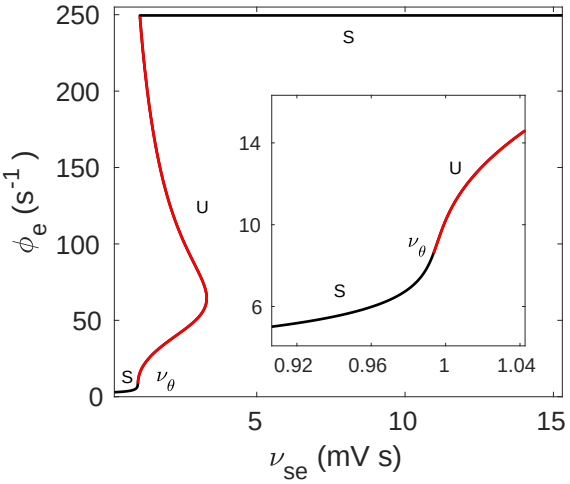

Fig 16. (color online) Steady states solution of the corticothalamic system for the variation of ν_{se} for tonic-clonic seizure. Black lines and the letter 'S' represent the stable steady state, and red lines and the letter 'U' represent the unstable steady states. Here ν_θ is the threshold value when the stable steady state becomes unstable. The inset shows zoomed view of the area around ν_θ.

In this paper, we ramp the coupling strength ν_{se} from an initial value ν_0 to a maximum value $\nu_{\max}$ and back to see the impact of the ramp characteristics on tonic-clonic seizures, with [33]

$$\nu_{se} = \nu_0 + (\nu_{\max} - \nu_0)\left[\frac{f(t) - f_{\min}}{f_{\max} - f_{\min}}\right], \tag{19}$$

$$f(t) = \tan^{-1}\left[\frac{t - t_1}{\Delta}\right] - \tan^{-1}\left[\frac{t - t_2}{\Delta}\right], \tag{20}$$

where t is the time. The ramp rise is centered on t_1, and the ramp fall is centered on t_2, and Δ is the characteristic rise time. Now, $0 \leqslant f(t) \leqslant \pi$, so we normalize by dividing by $f_{\max} - f_{\min}$ as seen in Eq. (19), where $f_{\max}$ and $f_{\min}$ are the maximum and minimum values of $f(t)$ actually encountered in a given instance.

Numerical Methods

We use *NFTsim* [44] to solve Eqs (11) – (17) numerically for the spatially uniform case in which the ∇^2 term in Eq. (14) is zero. To vary ν_{se} temporally, we use Eqs (19) and (20). This involves solving ordinary delay differential equations, because there is a

Table 1. Nominal parameters of the neural field model from [3].

Parameter	Value	Unit	Meaning
ν_{ee}	1.2	mV s	Excitatory corticocortical connectivity
ν_{ei}	-1.8	mV s	Inhibitory corticocortical connectivity
ν_{es}	1.4	mV s	Specific thalamic to cortical connectivity
ν_{re}	0.2	mV s	Cortical to thalamic reticular connectivity
ν_{rs}	0.2	mV s	Specific to reticular thalamic connectivity
ν_{se}	1.0	mV s	Cortical to specific thalamic connectivity
ν_{sr}	-1.0	mV s	Reticular to specific thalamic connectivity
$\nu_{sn}\phi_n$	2.0	mV	Subthalamic input
$Q_{\max}$	250	s^{-1}	Maximum firing rate
θ	15	mV	Mean neuronal threshold
σ	6	mV	Threshold standard deviation
γ_e	100	s^{-1}	Damping rate
α	60	s^{-1}	Decay rate of membrane potential
β	240	s^{-1}	Rise rate of membrane potential
t_0	80	ms	Corticothalamic return time (complete loop)
t_1	100	s	Center of the ramp rise
t_2	200	s	Center of the ramp fall
$\nu_{\max}$	1.2	mV s	Maximum value of ν_{se}
ν_0	0.8	mV s	Minimum value of ν_{se}
Δ	10	s	Characteristic rise time

propagation time delay $t_0/2$ between the different neural populations present in Eqs (15) and (17). Hence, a fourth-order Runge-Kutta integration is employed to solve these equations, with an integration time step of 10^{-4} s and store time histories of the delay terms $t_0/2$ into the past.

Because extensive comparisons with experiment have demonstrated that the normal brain operates close to stable fixed points [3, 8, 18, 30, 32], we start our simulations from a corticothalamic steady state with low firing rate. However, because of the delay time $t_0/2$, we must specify these initial steady-state conditions to apply for times $-t_0/2 < t \leqslant 0$.

We use the parameters in Table 1 as the initial parameters, which are taken from [3] with $\nu_0 = 0.8$ mV s in all cases. A constant input $\nu_{sn}\phi_n = 2$ mV is used and no external noise is applied in the simulations as the seizure onset occurs spontaneously. Simulations are 300 s long, and we record the output time series every 5 ms. For all simulations, we use the default parameters shown in Table 1 unless otherwise specified. The default parameters we used are the corresponding parameter set of [3] for tonic-clonic seizure which push the system into the vicinity of alpha instability. For the dynamic spectrum and power spectrum analysis, we employ the FFT (fast Fourier transform) algorithm with a Hanning window of 600 data points with an overlap of 200 points and sampling frequency of 200 Hz.

Acknowledgments

This work was supported by the Australian Research Council Center of Excellence for Integrative Brain Function (ARC Center of Excellence Grant CE140100007) and by an Australian Research Council Laureate Fellowship (Grant FL140100025).

References

1. Engel J, Pedley TA. Epilepsy: A comprehensive textbook. vol. 1. Lippincott-Raven, Philadelphia; 1997.
2. Browne TR, Holmes GL. Handbook of epilepsy. Lippincott Williams & Wilkins, Philadelphia; 2000.
3. Breakspear M, Roberts JA, Terry JR, Rodrigues S, Mahant N, Robinson PA. A unifying explanation of primary generalized seizures through nonlinear brain modeling and bifurcation analysis. Cereb Cortex. 2006;16(9):1296–1313.
4. Marten F, Rodrigues S, Benjamin O, Richardson MP, Terry JR. Onset of polyspike complexes in a mean-field model of human electroencephalography and its application to absence epilepsy. Philos Trans R Soc A. 2009;367(1891):1145–1161.

5. Roberts JA, Robinson PA. Modeling absence seizure dynamics: implications for basic mechanisms and measurement of thalamocortical and corticothalamic latencies. J Theor Biol. 2008;253(1):189–201.

6. Rodrigues S, Barton D, Szalai R, Benjamin O, Richardson MP, Terry JR. Transitions to spike-wave oscillations and epileptic dynamics in a human cortico-thalamic mean-field model. J Comput Neurosci. 2009;27(3):507–526.

7. Kim JW, Robinson PA. Compact dynamical model of brain activity. Phys Rev E. 2007;75(3):031907.

8. Robinson PA, Rennie CJ, Rowe DL. Dynamics of large-scale brain activity in normal arousal states and epileptic seizures. Phys Rev E. 2002;65(4):041924.

9. Chen M, Guo D, Wang T, Jing W, Xia Y, Xu P, et al. Bidirectional control of absence seizures by the basal ganglia: a computational evidence. PLoS Comput Biol. 2014;10(3):e1003495.

10. Velazquez JLP, Dominguez LG, Gaetz W, Cheyne D, Snead III OC, Wennberg R. Fluctuations in phase synchronization in brain activity: physiological interpretations of phase locking patterns. In: Topical Problems of Nonlinear Wave Physics. International Society for Optics and Photonics; 2006. p. 597510.

11. Lytton WW, Orman R, Stewart M. Computer simulation of epilepsy: implications for seizure spread and behavioral dysfunction. Epilepsy Behav. 2005;7(3):336–344.

12. Jirsa VK, Stacey WC, Quilichini PP, Ivanov AI, Bernard C. On the nature of seizure dynamics. Brain. 2014;137(8):2210–2230.

13. Dodrill CB. Correlates of generalized tonic-clonic seizures with intellectual, neuropsychological, emotional, and social function in patients with epilepsy. Epilepsia. 1986;27(4):399–411.

14. Andrew RD. Seizure and acute osmotic change: clinical and neurophysiological aspects. J Neurol Sci. 1991;101(1):7–18.

15. Hall D, Kuhlmann L. Mechanisms of seizure propagation in 2-dimensional centre-surround recurrent networks. PLoS One. 2013;8(8):e71369.

16. Kramer MA, Truccolo W, Eden UT, Lepage KQ, Hochberg LR, Eskandar EN, et al. Human seizures self-terminate across spatial scales via a critical transition. Proc Natl Acad Sci USA. 2012;109(51):21116–21121.

17. Staley K. Molecular mechanisms of epilepsy. Nature Neurosci. 2015;18(3):367.

18. Robinson PA, Rennie CJ, Rowe DL, O'Connor SC. Estimation of multiscale neurophysiologic parameters by electroencephalographic means. Hum Brain Mapp. 2004;23(1):53–72.

19. Yang DP, Robinson PA. Critical dynamics of Hopf bifurcations in the corticothalamic system: Transitions from normal arousal states to epileptic seizures. Phys Rev E. 2017;95(4):042410.

20. Kim JW, Roberts JA, Robinson PA. Dynamics of epileptic seizures: evolution, spreading, and suppression. J Theor Biol. 2009;257(4):527–532.

21. Deco G, Jirsa VK, Robinson PA, Breakspear M, Friston KJ. The dynamic brain: from spiking neurons to neural masses and cortical fields. PLoS Comput Biol. 2008;4(8):e1000092.

22. Pinotsis DA, Moran RJ, Friston KJ. Dynamic causal modeling with neural fields. NeuroImage. 2012;59(2):1261–1274.

23. Nunez PL. The brain wave equation: A model for the EEG. Math Biosci. 1974;21(3-4):279–297.

24. Freeman WJ. Mass action in the nervous system. Academic Press, New York; 1975.

25. Jirsa VK, Haken H. Field theory of electromagnetic brain activity. Phys Rev Lett. 1996;77(5):960–963.

26. Robinson PA, Rennie CJ, Wright JJ. Propagation and stability of waves of electrical activity in the Cereb. Cortex. Phys Rev E. 1997;56(1):826.

27. Rennie CJ, Robinson PA, Wright JJ. Unified neurophysical model of EEG spectra and evoked potentials. Biol Cybern. 2002;86(6):457–471.

28. Robinson PA, Whitehouse RW, Rennie CJ. Nonuniform corticothalamic continuum model of electroencephalographic spectra with application to split-alpha peaks. Phys Rev E. 2003;68(2):021922.

29. van Albada SJ, Kerr CC, Chiang AKI, Rennie CJ, Robinson PA. Neurophysiological changes with age probed by inverse modeling of EEG spectra. Clin Neurophysiol. 2010;121(1):21–38.

30. Abeysuriya RG, Rennie CJ, Robinson PA. Physiologically based arousal state estimation and dynamics. J Neurosci Methods. 2015;253:55–69.

31. Breakspear M, Terry JR, Friston KJ. Modulation of excitatory synaptic coupling facilitates synchronization and complex dynamics in a biophysical model of neuronal dynamics. Network: Comp Neural Sci. 2003;14(4):703–732.

32. Abeysuriya RG, Rennie CJ, Robinson PA. Prediction and verification of nonlinear sleep spindle harmonic oscillations. J Theor Biol. 2014;344:70–77.

33. Deeba F, Sanz-Leon P, Robinson PA. Dependence of absence seizure dynamics on physiological parameter evolution. J Theor Biol. 2018;454:11–21.

34. Deeba F, Sanz-Leon P, Robinson PA. Unified dynamics of interictal events and absence seizures. Phys Rev E. 2019;100(2):022407.

35. Schiff SJ, Colella D, Jacyna GM, Hughes E, Creekmore JW, Marshall A, et al. Brain chirps: spectrographic signatures of epileptic seizures. Clin Neurophysiol. 2000;111(6):953–958.

36. Jiruska P, De Curtis M, Jefferys JGR, Schevon CA, Schiff SJ, Schindler K. Synchronization and desynchronization in epilepsy: controversies and hypotheses. J Physiol. 2013;591(4):787–797.

37. Schiff SJ, Milton JG, Heller J, Weinstein SL. Wavelet transforms and surrogate data for electroencephalographic spike and seizure localization. Optical Engineering. 1994;33(7):2162–2170.

38. Soltesz I, Staley K. Computational neuroscience in epilepsy. Academic Press; 2011.

39. Köppen M, Kasabov N, Coghill G. Advances in Neuro-Information Processing: 15th International Conference, ICONIP 2008, Auckland, New Zealand, November 25-28, 2008, Revised Selected Papers. vol. 5507. Springer; 2009.

40. Tzallas AT, Tsipouras MG, Fotiadis DI. Epileptic seizure detection in EEGs using time–frequency analysis. IEEE Trans Inf Technol Biomed. 2009;13(5):703–710.

41. Cohen L. Time-frequency distributions-a review. Proc IEEE. 1989;77(7):941–981.

42. Liley DTJ, Cadusch PJ, Wright JJ. A continuum theory of electro-cortical activity. Neurocomputing. 1999;26:795–800.

43. Braitenberg V, Schüz A. Cortex: statistics and geometry of neuronal connectivity. Springer Science & Business Media; 2013.

44. Sanz-Leon P, Robinson PA, Knock SA, Drysdale PM, Abeysuriya RG, Fung PK, et al. NFTsim: theory and simulation of multiscale neural field dynamics. PLoS Comput Biol. 2018;14(8):e1006387.